Optics Letters

Reflective binary amplitude grating for soft x-ray shearing and Hartmann wavefront sensing

Kenneth A. Goldberg,[1,*] Diane Bryant,[1] Antoine Wojdyla,[1] Michael Helmbrecht,[2] and Eric Gullikson[3]

[1]Advanced Light Source, Lawrence Berkeley National Laboratory, 1 Cyclotron Road, Berkeley, California 94720, USA
[2]A.M. Fitzgerald & Associates, LLC, 700 Airport Blvd., Suite 210, Burlingame, California 94010, USA
[3]Center for X-Ray Optics, Lawrence Berkeley National Laboratory, 1 Cyclotron Road, Berkeley, California 94720, USA
*Corresponding author: KAGoldberg@lbl.gov

Received 27 May 2020; revised 17 July 2020; accepted 17 July 2020; posted 17 July 2020 (Doc. ID 398737); published 18 August 2020

We demonstrate a reflective wavefront sensor grating suitable for the characterization of high-quality x-ray beamlines and optical systems with high power densities. Operating at glancing incidence angles, the optical element is deeply etched with a two-level pattern of shearing interferometry gratings and Hartmann wavefront sensor grids. Transverse features block unwanted light, enabling binary amplitude in reflection with high pattern contrast. We present surface characterization and soft x-ray reflectometry of a prototype grating array to demonstrate function prior to wavefront measurement applications. A simulation of device performance is shown.

https://doi.org/10.1364/OL.398737

A new generation of high-brightness, coherent, short-wavelength synchrotron and free electron laser (FEL) light sources is driving x-ray optical system requirements to preserve the wavefront quality from the source to the sample. Wavefront sensor feedback is essential for the control and optimization of x-ray beamlines with diffraction-limited performance.

Aberrations accrue from every optical element in the beamline. With soft and tender x-ray wavelengths ranging from 0.1 nm to 10 nm, the wavefront quality is measured in fractions of a nanometer. This includes contributions from mirror surface figure errors, misalignment, thermal and mechanical distortions, surface contamination, and vibration. For diffractive optical elements, including monochromator gratings and crystals, wavefront quality is affected by line-placement errors as well as substrate quality and distortion. Inhomogeneities in transmission elements can also introduce wavefront phase and amplitude errors.

Feedback for correcting aberrations begins with accurate measurements from wavefront sensors. Among the many techniques that have been reported for soft and tender x-ray applications, shearing interferometry (frequently called *Talbot interferometry*) [1–5] and Hartmann sensing [6,7] have emerged as the most commonly applied approaches for high accuracy and sensitivity. Their widespread use can be attributed to the fact that they are straightforward to implement, and the measurements can be recorded and analyzed without great effort or computational power. Shearing and Hartmann share similar hardware requirements. Both techniques probe the local wavefront slope, enabling wavefront reconstruction. However, they operate on different principles.

Shearing is an interferometric technique that uses a 1D or 2D grating structure to produce multiple, laterally displaced and overlapping copies of the wavefront at a downstream detection plane. It relies on the beam coherence and on Talbot self-imaging properties to produce high-contrast fringes. In shearing, optimal separation distances between the grating and the detection plane are dependent on the wavelength and the grating pitch: maintaining a fixed separation distance across a wide energy range can require the use of several gratings. In principle, the shearing grating can be made from any periodic phase or amplitude structure. Due to differences in material attenuation properties, transmission *phase* structures are commonly used at hard x-ray wavelengths [8], and transmission *amplitude* structures at soft x-ray wavelengths [1,3].

Hartmann testing is a non-interferometric technique in which a well-characterized grid of holes in an opaque screen projects a 1D or 2D array of spots or lines, with diffraction, onto the detection plane. The grid is designed so the projected spots are distinct and not overlapping. Similar to shearing, when a fixed grid-to-detection-plane separation is used, the optimal grid pitch and hole size are wavelength dependent. To achieve high a signal-to-noise ratio, it is important that the Hartmann grid be opaque in the blocked regions.

Between these two complementary and compatible approaches, Hartmann has greater capacity to measure large aberrations, while shearing offers tunable high sensitivity for small aberrations and a higher measurement point density.

While both approaches are proven and effective, developing wavefront sensors for high-coherent-flux beamlines presents challenges that have forced us to consider alternative implementations. The most significant issue is high power and power density; and the second is small beam width, below 1 mm in some cases.

To our knowledge, all shearing and Hartmann applications on soft x-ray beamlines have used transmission elements made with patterned thin foils (Hartmann) or absorber-coated membranes (shearing)—Si or Si_3N_4—with ~1 μm thickness. For

our applications, we calculate that due to poor thermal conductivity, absorbing approximately 0.5 W in 1 mm^2, in a 3 mm wide membrane, would increase membrane temperatures by hundreds to thousands of degrees [9], melting them. Therefore, an alternative, thermally robust mechanism for wavefront sensor gratings must be developed for the new generation of beamlines.

Gratings used at glancing incidence are a common feature in x-ray monochromators where they serve as a dispersive element, enabling energy selection and filtering. Small angles of incidence spread the beam footprint in the tangential direction (the direction of propagation), reducing the power density. Thick substrates promote heat dissipation and active cooling, where necessary. However, monochromator grating structures, whether they are blazed or lamellar, primarily modify the phase of the beam by encoding spatially varying path lengths. Amplitude modulation for those gratings is a secondary consideration connected to the diffraction efficiency. It can arise from shadowing in the 3D structure.

Phase-shifting properties can be adapted to reflection-mode shearing gratings using a height-relief structure. Gratings would function like transmission phase gratings at normal incidence, but would use an off-axis detector geometry (Fig. 1). The phase change upon reflection from a surface of depth h is [10]

$$\Delta\phi = \frac{4\pi}{\lambda} h \sin\theta. \quad (1)$$

Wavelength dependence complicates fabrication significantly, forcing a range of etch depths to be used. For wavelengths from 0.5 nm to 5 nm, with 1° incidence, achieving $\pi/4$ phase shift (for example) requires depths from 1.8 nm to 18 nm—challenging to achieve on a single device. However, most importantly, creating *amplitude* modulation with high contrast and opacity for Hartmann testing requires a different grating structure: unwanted light must be redirected or blocked.

Our solution is to deeply etch a binary pattern that includes a series of regularly spaced horizontal walls as barriers, to intercept and block light (Fig. 2). Light reflected from the top surface of the structure propagates onward, while the transverse walls intercept all other rays, either directly, or after reflection from the lower surface.

The relationship between the largest angle of incidence, θ, the tangential distance between walls, L, and the minimum wall depth, a, arises from the path of the extreme ray [Fig. 2(c)]: the ray that just clears the wall on the left. To block the incident rays that miss the top surface, we require $a > (1/2)L\tan\theta$ (typically, $a > 10$ μm). A ray-optics approach is justified with

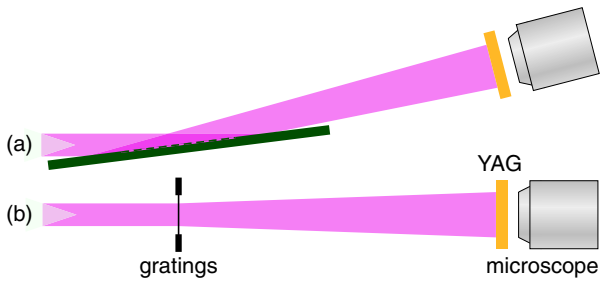

Fig. 1. Schematic shearing and Hartmann wavefront sensor geometries with the grating (a) in reflection and (b) in transmission. In practice, the reflection-grating length will be small relative to the distance from the grating to the detection plane. A microscope and camera system are described in Ref. [4].

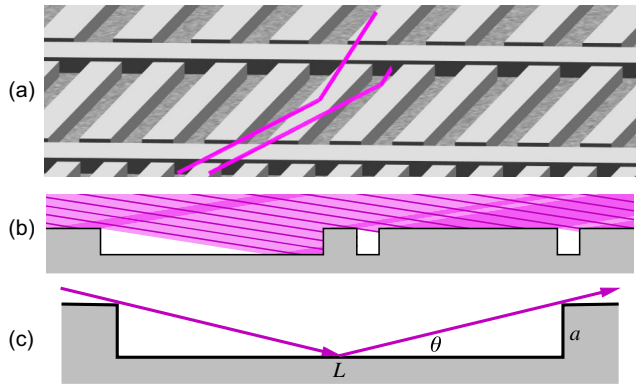

Fig. 2. (a) 3D pattern detail showing glancing rays reflected or blocked. (b) Sagittal cross section of two grating regions illuminated from the upper left. Only light reflected from the top surface propagates onward; walls block all other light. (c) Trajectory of the extreme ray shows geometry for determining the minimum wall height given L and θ.

pattern sizes ranging from 10^3 to 10^6 larger than the maximum wavelength. A deeper etch allows the spacing between walls to be increased. Glancing-incidence effectively foreshortens the pattern in the tangential direction, reducing the effective feature sizes by a factor $\sin\theta$, which is 1/57.3 at 1°. Light reflected from the top surface of the walls appears weak in the recorded images, but having no horizontal features, it does not degrade the measurement of 1D grating patterns. Here, a 198 μm wide wall diffracts light like a 3.5 μm slit. For soft x-ray photon energies, a 10 μm wide wall would be sufficiently opaque: it would diffract like an 174 nm slit, and would occupy less than 1.0% of the pattern area.

1D and 2D gratings can be designed using this approach, with the pattern elongated in the tangential direction to accommodate the glancing angle of incidence. Our prototype will provide 1D wavefront-correction feedback for a bendable, glancing-incidence adaptive x-ray mirror that is capable of tangential shape adjustment. As such, the pattern contains only 1D shearing gratings and Hartmann grids. Note that for 2D patterns, the walls could be incorporated into the useful aspects of the design.

Surface quality is a significant consideration only for the top level where the device functions as an x-ray mirror. This is further discussed below. The quality of the lower surface is of little consequence because light reflected from that region is blocked by the walls. However, since unwanted light scattered from roughness on the lower surface could reach a downstream detector, increasing the wall height can provide greater angular separation and scattered light mitigation.

A photograph of a grating array chip is shown in Fig. 3. Gratings 3 mm wide exceed the beam width in our application. In the tangential direction, the beam illuminates a column of 10 gratings or grids all at once. Each grating's pitch is optimized for a different central wavelength. A full column of illuminated patterns will be projected onto the detector plane, to appear in the recorded image; the appropriate wavelength-matched grating or grid can then be selected from the array for analysis.

In this grating array, the three left columns contain 10 shearing gratings each. The fourth column contains eight Hartmann grids and a test region, described below. The fifth column is a

blank, mirror region. The gratings and grids are designed for a fixed grating-to-detector distance of approximately 300 mm. At glancing incidence, this is a conical diffraction geometry. The shearing gratings have 50% duty cycle (i.e., equal lines and spaces) and pitch values from 49 μm to 16 μm to span the photon energy range of 170 eV − 1583 eV (7.29 nm to 0.78 nm wavelength). The Hartmann grids have a duty cycle of 22.5% and span the same range.

While they are designed for specific energies, the individual grids and gratings can operate over narrow bands [4]. Our studies show that in this design, Hartmann grids can operate 17.5% below the design energy before adjacent beamlets overlap. Owing to the Talbot condition, the usable range for amplitude-modulating shearing gratings is closer to ±4%. This issue should be addressed, case by case, for alternate designs.

Shearing grating design [2–5] and Hartmann grid design [4,6] have been described by several groups, including the approach of using an array of gratings in transmission, and utilizing fractional Talbot planes. Using multiple Talbot planes from individual gratings at different energies can reduce the number of unique gratings required in an array.

Gratings were fabricated from single-side-polished, prime-grade, 675 μm thick, silicon wafers. Patterns were transferred using a deep-ultraviolet photolithography stepper, followed by reactive ion etching to strip a thermal oxide hard mask, and a deep reactive-ion etch to achieve depths greater than 20 μm [11].

White light interferometry was used to characterize the surface topography in the clear areas and the etched regions (Fig. 4). Observed rms and peak-to-valley (PV) variations in 100 × 50 μm regions are shown. The etched regions reach a depth of approximately 29 μm in the wide areas, and 25.6 μm between the grating lines. With the prototype's 1.067 mm between horizontal walls (L) and 1° angle of incidence (θ), this depth exceeds the minimum requirement $[(1/2)L\tan\theta]$ of 9.3 μm by a factor of 2.75.

Each 3 × 1 mm grating is intended to be interpreted separately during 1D wavefront measurements, and thus surface quality requirements apply locally to these small regions. Furthermore, small, tangential slope errors will not distort the 1D fringe patterns. For 1° incidence, achieving an uncalibrated $\lambda/20$ rms path length error upon reflection (for example) requires a surface quality of $\sigma = 1.43\lambda$. Thus, 1 nm surface roughness would meet this requirement for wavelengths down to 0.7 nm (1771 eV).

2D wavefront measurements would require high surface quality to be achieved—or the device to be calibrated—across the full beam footprint.

The device was measured with soft x-ray light at the Advanced Light Source. Glancing-incidence reflectance reveals the efficacy of the binary amplitude structure in blocking the unwanted light. The monochromatic beam ($E/\Delta E$=1000) has a spot size of 120 × 40 μm at focus. Using a 2 mm photodiode to detect the reflected power, the beam was vertically centered on the horizontal wall between two identical grating regions and scanned across the pattern (Fig. 5). The size of the tangential beam footprint changed as the angle of incidence was varied from 1° to 4°.

The five regions of the test-grating pattern have constant 32 μm pitch and duty cycle values varying from 0% (dark) to 100% (bright). Measurements were made at photon energies 500 eV (2.48 nm) and 750 eV (1.65 nm). While the prototype was designed to operate at 1°, we measured with incidence angles from 1° to 4° to test the useful operating range.

The scan data were analyzed in the following way. Reflection from the top of the wall produces a constant light-background signal that is measured in the 0% duty-cycle region; that signal defines the *zero* point and is subtracted from the others. The signal from the center of the 100% duty-cycle region defines the *maximum* value, used to normalize the measurements. The scaled signal recorded at the center of each of the three gratings then reveals the reflected fraction, which should follow the duty cycle if the device is effectively blocking unwanted light (Fig. 6).

For the two photon energies, 500 eV and 750 eV, respectively, the attenuation lengths in Si are 0.43 μm and 1.22 μm [12], and in the unpatterned area, the measured reflectivities at 1° are 0.841 ± 0.002 and 0.845 ± 0.002.

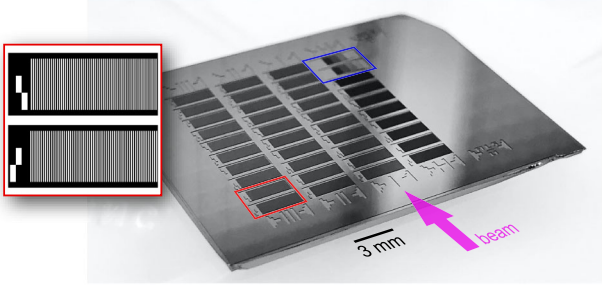

Fig. 3. Photograph of etched patterns on a grating chip cleaved from a 152-mm Si wafer. The die has 38 individual 3 × 1 mm gratings and an open mirror area. A pattern detail (red outline) shows two gratings with alignment marks. Etched regions are shown in black. Test gratings designed for reflectometry are outlined in blue and described in Fig. 5.

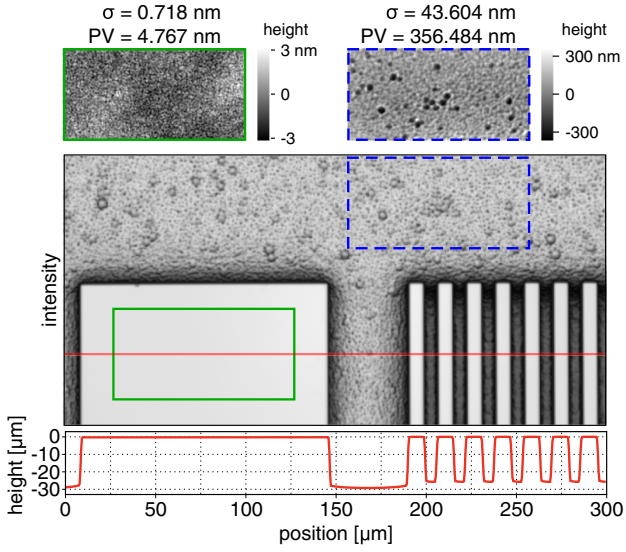

Fig. 4. Surface characterization with white-light interferometry. The intensity image (central portion) shows a pattern of etched regions surrounding protected top-surface areas. The grating lines have 16 μm pitch. Individually scaled surface height map details (100 × 50 μm) are extracted from the clear area (green outline) and from the etched region (blue dash). A cross-sectional height plot is calculated from a vertical average over 50 μm, centered about the red line. The contour is plotted isometrically, to show the depth relative to the lateral size.

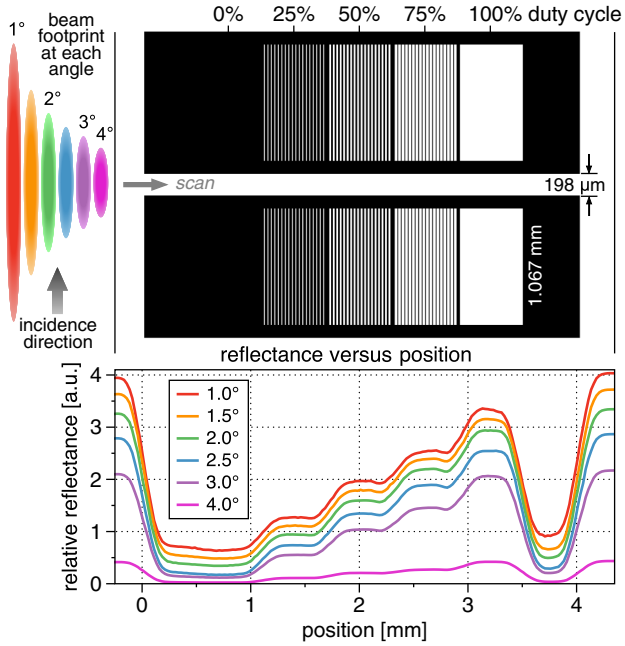

Fig. 5. Grating test region with etched areas in black. Gratings have constant pitch and five duty-cycle values. Approximate footprints of the focused soft x-ray beams are shown for six angles of incidence. Reflected power is measured as the beam is scanned horizontally across the pattern. For 500 eV photon energy, relative reflectance for six incidence angles is shown, aligned with the gratings, above; the critical angle is 3.48° [12].

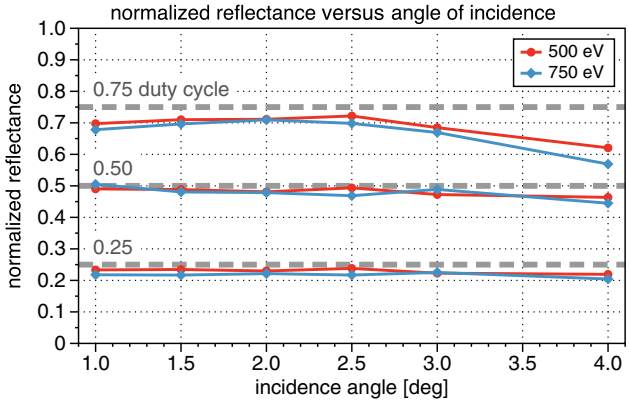

Fig. 6. Reflected light fraction from the 25%, 50%, and 75% duty-cycle gratings, extracted from the scans (Fig. 5) and plotted versus angle of incidence. The design angle is 1°. Maximum uncertainty is 0.7% for 750 eV and 1.0% for 500 eV.

A coherent wave model (Fig. 7) demonstrates shearing interferometry of a 1.267 nm wavelength Gaussian beam at 1° incidence. The transverse intensity FWHM is 833 μm. Of the 10 different gratings, the Talbot condition is met in the fifth row from the bottom, with 19.5 μm pitch, 300 mm downstream.

This work demonstrates glancing incidence reflection x-ray gratings with binary amplitude modulation, made with deep etching and pattern features that block unwanted light. These optical elements are well suited for shearing interferometry gratings and Hartmann wavefront sensor grids, and possibly structured illumination, and arbitrary holographic

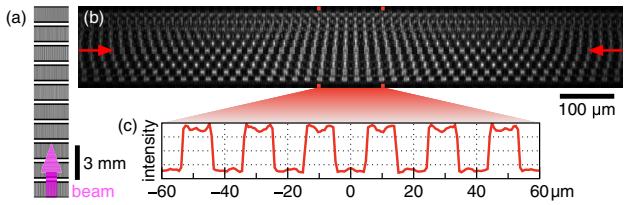

Fig. 7. Coherent model of a recorded shearing interferogram at 1.267 nm wavelength, from the array's third column. (a) 10-row grating pattern: etched regions are shown in black. (b) Central 1 mm interferogram detail. Red arrows mark the row where the intensity cross section (c) is extracted. The 1° incidence angle accounts for foreshortening by a factor of 57.3.

or diffraction-pattern applications where the incident beam's power density is too high for thin transmission elements. Arrays of features enable the devices to be used across a broad energy range.

Funding. U.S. Department of Energy (DE-AC02-05CH11231).

Acknowledgment. This work was supported by the Director, Office of Science, Office of Basic Energy Sciences, of the U.S. Department of Energy under Contract No. DE-AC02-05CH11231. The authors appreciate the support of Howard Padmore and Elaine DiMasi of LBNL. Daniel Contreras and Min He of AMFitzgerald fabricated the gratings. Ian Lacey of LBNL assisted with surface metrology.

Disclosures. The authors declare no conflicts of interest.

REFERENCES

1. P. P. Naulleau, K. A. Goldberg, and J. Bokor, J. Vac. Sci. Technol. B **18**, 2939 (2000).
2. S. Matsuyama, H. Yokoyama, R. Fukui, Y. Kohmura, K. Tamasaku, M. Yabashi, W. Yashiro, A. Momose, T. Ishikawa, and K. Yamauchi, Opt. Express **20**, 24977 (2012).
3. D. J. Merthe, V. V. Yashchuk, K. A. Goldberg, M. Kunz, N. Tamura, W. R. McKinney, N. A. Artemiev, R. S. Celestre, G. Y. Morrison, E. H. Anderson, B. V. Smith, E. E. Domning, S. B. Rekawa, and H. A. Padmore, Opt. Eng. **52**, 033603 (2013).
4. A. Wojdyla, D. Bryant, W. Chao, L. Assoufid, D. Cocco, M. Idir, and K. A. Goldberg, Proc. SPIE **10760**, 1076003 (2018).
5. M. Seaberg, R. Cojocaru, S. Berujon, E. Ziegler, A. Jaggi, J. Krempasky, F. Seiboth, A. Aquila, Y. Liu, A. Sakdinawat, H. J. Lee, U. Flechsig, L. Patthey, F. Koch, G. Seniutinas, C. David, D. Zhu, L. Mikeš, M. Makita, T. Koyama, A. P. Mancuso, H. N. Chapman, and P. Vagovič, J. Synchrotron. Radiat. **26**, 1115 (2019).
6. P. Mercère, P. Zeitoun, M. Idir, S. Le Pape, D. Douillet, X. Levecq, G. Dovillaire, S. Bucourt, K. A. Goldberg, P. P. Naulleau, and S. Rekawa, Opt. Lett. **28**, 1534 (2003).
7. M. Idir, P. Mercere, M. H. Modi, G. Dovillaire, X. Levecq, S. Bucourt, L. Escolano, and P. Sauvageot, Nucl. Instrum. Methods Phys. Res. A **616**, 162 (2010).
8. S. Marathe, X. Shi, M. J. Wojcik, N. G. Kujala, R. Divan, D. C. Mancini, A. T. Macrander, and L. Assoufid, Opt. Express **22**, 14041 (2014).
9. R. T. Balmer, *Modern Engineering Thermodynamics* (Academic, 2011).
10. E. L. Church and P. Z. Takacs, Opt. Eng. **34**, 353 (1995).
11. M. J. Madou, *Fundamentals of Microfabrication and Nanotechnology*, 3rd ed. (CRC Press, Taylor & Francis Group, 2012), Vol. **II**.
12. CXRO, "Index of refraction data," http://henke.lbl.gov/optical_constants/.